ATAD2 Drives Prostate Cancer Progression to Metastasis

Anindita Dutta[1], Antonio Rodriguez-Calero[2,3], Kacey Ronaldson-Bouchard[4], Anne Offermann[5], Daoud Rahman[1], Twinkle Bapuji Vhatkar[6], Dan Hasson[1,6,7,8], Mohammed Alshalalfa[9], Elai Davicioni[9], R. Jeffrey Karnes[10], Mark A. Rubin[2], Gordana Vunjak-Novakovic[4,11], Cory Abate-Shen[12,13,14,15,16], and Juan Martin Arriaga[1,7,17]

ABSTRACT

Metastasis accounts for the overwhelming majority of cancer deaths. In prostate cancer and many other solid tumors, progression to metastasis is associated with drastically reduced survival outcomes, yet the mechanisms behind this progression remain largely unknown. ATPase family AAA domain containing 2 (ATAD2) is an epigenetic reader of acetylated histones that is overexpressed in multiple cancer types and usually associated with poor patient outcomes. However, the functional role of ATAD2 in cancer progression and metastasis has been relatively understudied. Here, we employ genetically engineered mouse models of prostate cancer bone metastasis, as well as multiple independent human cohorts, to show that ATAD2 is highly enriched in bone metastasis compared with primary tumors and significantly associated with the development of metastasis. We show that ATAD2 expression is associated with MYC pathway activation in patient datasets and that, at least in a subset of tumors, MYC and ATAD2 can regulate each other's expression. Using functional studies on mouse bone metastatic cell lines and innovative organ-on-a-chip bone invasion assays, we establish a functional role for ATAD2 inhibition in reducing prostate cancer metastasis and growth in bone.

Implications: Our study highlights ATAD2 as a driver of prostate cancer progression and metastasis and suggests it may constitute a promising novel therapeutic target.

Introduction

Prostate cancer is a heterogeneous disease in which prognosis is highly impacted by the development of metastasis (1). This occurs mainly in bones and entails high patient morbidity and mortality (2–4). Identifying the factors that determine metastasization of prostate cancer to bone is thus of utmost importance for risk stratification and disease management, as well as for designing novel therapeutic strategies. Progression to metastatic disease is most frequently observed after local therapy and subsequent androgen deprivation, termed metastatic castration-resistant prostate cancer. In a minority of patients (5%–10%), metastasis may be evident before androgen deprivation (termed metastatic hormone-sensitive disease) either at diagnosis ("*de novo*," synchronous metastatic disease) or after local therapy (metachronous metastatic disease; refs. 5, 6). The mechanisms behind this progression are likely multifactorial and many remain largely unknown (7–9). Genetically engineered mouse models (GEMM) have provided multiple cues into how this progression occurs (10–12). These models allow the study of spontaneous cancer development and progression in a genetically controlled system, including in immunologically intact whole organisms. We and others have shown in multiple models that genetic alterations may be necessary for cancer to progress to metastatic disease, yet other factors cooperate to ultimately determine metastasis outcomes. These include cell-intrinsic activation of critical transcriptional modulators (i.e., MYC, ETV4, and CITED2; refs. 13–17) and signaling pathways (i.e., NF-κB, Wnt, and MAPK; refs. 18–21), as well as expansion of stromal cell subtypes (22, 23).

Expression of ATPase family AAA domain containing 2 (ATAD2) has been linked to tumor progression and metastasis in multiple tumor types (24–26). However, except for a few studies in lung metastasis (27, 28), proof of its functional regulation of metastasis is largely lacking. ATAD2 functions as an epigenetic reader of acetylated histones (26, 29, 30) and is considered a modulator of the transcriptional activity of multiple transcription factors, including oncogene MYC and the androgen receptor (AR; refs. 31, 32), both being critical regulators of prostate cancer progression.

[1]Department of Oncological Sciences, Icahn School of Medicine at Mount Sinai, New York, New York. [2]Department for BioMedical Research, University of Bern, Bern, Switzerland. [3]Institute of Pathology, University of Bern, Bern, Switzerland. [4]Department of Biomedical Engineering, Columbia University, New York, New York. [5]Institute of Pathology, Universitätsklinikum Schleswig-Holstein, Kiel, Germany. [6]Bioinformatics for Next Generation Sequencing Shared Resource Facility, Tisch Cancer Institute, Icahn School of Medicine at Mount Sinai, New York, New York. [7]Tisch Cancer Institute, Icahn School of Medicine at Mount Sinai, New York, New York. [8]Black Family Stem Cell Institute and Center for Advancement of Blood Cancer Therapies, Icahn School of Medicine at Mount Sinai, New York, New York. [9]Veracyte, Inc., South San Francisco, California. [10]Department of Urology, Mayo Clinic, Rochester, Minnesota. [11]Department of Medicine, Vagelos College of Physicians and Surgeons, Herbert Irving Comprehensive Cancer Center, Columbia University Irving Medical Center, New York, New York. [12]Department of Molecular Pharmacology and Therapeutics, Herbert Irving Comprehensive Cancer Center, Columbia University Irving Medical Center, New York, New York. [13]Department of Urology, Herbert Irving Comprehensive Cancer Center, Columbia University Irving Medical Center, New York, New York. [14]Department of Medicine, Herbert Irving Comprehensive Cancer Center, Columbia University Irving Medical Center, New York, New York. [15]Department of Pathology and Cell Biology, Herbert Irving Comprehensive Cancer Center, Columbia University Irving Medical Center, New York, New York. [16]Department of Systems Biology, Herbert Irving Comprehensive Cancer Center, Columbia University Irving Medical Center, New York, New York. [17]Department of Urology, Icahn School of Medicine at Mount Sinai, New York, New York.

Corresponding Authors: Juan Martin Arriaga, Department of Oncological Sciences and Urology, Icahn School of Medicine at Mount Sinai, New York, NY 10029. E-mail: juan.arriaga@mssm.edu; and Cory Abate-Shen, Departments of Molecular Pharmacology and Therapeutics, Urology, Medicine, Pathology & Cell Biology, and Systems Biology, Herbert Irving Comprehensive Cancer Center, Columbia University Irving Medical Center, New York, NY 10032. E-mail: cabateshen@columbia.edu

Mol Cancer Res 2025;23:379–90

doi: 10.1158/1541-7786.MCR-24-0544

Although its precise biological function is still unclear, in prostate cancer, ATAD2 is regulated by androgens and may, in turn, interact with AR to modulate its signaling in favor of cancer cell survival (32, 33). Moreover, ATAD2 may affect the epigenetic landscape of prostate tumors by favoring open chromatin conformations that are enriched upon cancer progression (34), as well as through regulation of other key epigenetic modulators, such as EZH2 (35).

Previous studies including our own have put forward MYC as a critical regulator of both early and late progression of prostate cancer (13, 15, 36, 37). Indeed, using a unique GEMM that enables quantitative studies on progression of prostate cancer to bone metastasis, we found MYC to be necessary but not sufficient for metastasis. Furthermore, based on integration of transcriptional profiles in this model and in human datasets, we have derived a gene signature downstream of MYC and RAS, called META16, that includes ATAD2 and is enriched in metastasis versus primary tumors, as well as associated with worse metastasis-free survival (15).

Given the clinical relevance of bone metastasis in prostate cancer, the incomplete understanding of its molecular mediators, and the lack of functional validation of the relevance of ATAD2 for metastasis, we studied whether ATAD2 drives prostate cancer progression to metastasis, including bone. By performing functional studies in human and mouse models and correlative studies on multiple human datasets, we show that ATAD2 is regulated by MYC, is consistently upregulated in metastasis compared with primary tumors, and that its inhibition is a promising therapeutic strategy for metastatic prostate cancer.

Materials and Methods

Mouse studies and analyses of GEMMs

All experiments using animals were performed according to protocols approved by the Institutional Animal Care and Use Committee at the Columbia University Irving Medical Center and Icahn School of Medicine at Mount Sinai. All mice were housed in pathogen-free barrier conditions under 12-hour light–dark cycles and with temperature and humidity set points at 20°C to 25°C and 30% to 70%, respectively. As our focus was prostate cancer, only male mice were used. *NP* (*Nkx3-1*^{CreERT2}; *Pten*$^{flox/flox}$; *R26R-CAG-*$^{LSL\text{-}EYFP/+}$, RRID: IMSR_JAX:033751) and *NPK* (*Nkx3-1*^{CreERT2}; *Pten*$^{flox/flox}$; *Kras*$^{LSL\text{-}G12D/+}$; *R26R-CAG-*$^{LSL\text{-}EYFP/+}$, *RRID*: IMSR_JAX:033761) mice were bred with a conditional EYFP reporter, as previously described (12, 15, 38). Mice were induced to form tumors at 2 to 3 months of age by administration of tamoxifen (Sigma-Aldrich) using 100 mg kg^{-1} (in corn oil) once daily for four consecutive days. Mice were euthanized when their body condition score was <1.5 or when they experienced body weight loss ≥20% or showed signs of distress, such as difficulty breathing or urinary obstruction, except *NP* mice which were dissected 1 year after induction.

Six- to eight-week-old male athymic nude-Foxn1^{nu} mice used for intracardiac studies were purchased from Envigo (RRID: IMSR_ENV:HSD-069), and NOD/SCID mice (NOD.CB17-Prkdcscid/J, strain 001303, RRID: IMSR_JAX:001303) used for intratibial studies were purchased from The Jackson Laboratory.

IHC

For histologic and IHC analyses, tissues were fixed in 10% formalin (Thermo Fisher Scientific). Bones were decalcified for 3 weeks in 15% EDTA (pH 7.0) solution (Sigma-Aldrich). Histopathologic and IHC analyses were conducted on 3-μm paraffin sections. Images were captured using an Olympus VS120 whole-slide scanning microscope. IHC was performed with citrate-based antigen retrieval (Vector Labs, H-330) using the VECTASTAIN Elite ABC-HRP Kit (Vector Labs, PK-6100). Antibodies used were anti–human ATAD2 ab244431 1/250 (Abcam Inc., RRID: AB_3674856) and anti–mouse ATAD2 cs50563 1/200 (Cell Signaling Technology Inc., RRID: AB_3674855).

Cell lines

22Rv1 (ATCC, CRL-2505, RRID: CVCL_1045), LNCaP (ATCC, CRL-1740, RRID: CVCL_0395), PC-3 (ATCC, CRL-1435, RRID: CVCL_0035), and DU145 cells (ATCC, HTB-81, RRID: CVCL_0105) were grown and maintained in RPMI-1640 (ATCC, 30-2001) supplemented with 10% FBS (Sigma-Aldrich), whereas HEK-293FT cells (Invitrogen, R700-07, RRID: CVCL_6911) were cultured in DMEM-10% FBS (Thermo Fisher Scientific). Cell lines were authenticated by short tandem repeat profiling, passaged twice weekly, used within 30 passages, and tested negative for *Mycoplasma* using the Universal Mycoplasma Detection Kit (ATCC, #30-1012K). Clonal cell derivatives capable of target gene overexpression by CRISPRactivation (CRISPRa) were generated as previously described (17).

Mouse *NP* and *NPK* cell lines were derived from advanced primary tumors of their respective genotypes, as described previously (15, 38), and grown in RPMI-1640 supplemented with 10% FBS.

RNA extraction and qRT-PCR analysis

RNA from cell lines was extracted with TRIzol reagent (Thermo Fisher Scientific, 15-596-026), reverse-transcribed with SuperScript III First-Strand Synthesis SuperMix (Thermo Fisher Scientific, 11-752-050), and RNA expression measured by qRT-PCR using the QuantiTect SYBR Green PCR kit (QIAGEN, 204145). Sequences of all primers used in this study are provided in Supplementary Table S2.

Western blotting

Total protein extracts were prepared by lysis of cells with 1× RIPA buffer [0.1% SDS, 1.0% deoxycholate sodium salt, 1.0% Triton X-100, 0.15 mol/L NaCl, 10 μmol/L Tris-HCl (pH 7.5), and 1 mmol/L EDTA] with fresh 1% protease inhibitor (Roche, #1697498), phenylmethylsulfonylfluoride (Sigma-Aldrich, 10837091001), and 1% phosphatase inhibitor (Sigma-Aldrich, #P2850). Protein lysates (20 μg per lane) were resolved by SDS-PAGE, followed by immunoblotting with primary antibodies anti–human ATAD2 ab244431 1/250 (Abcam), anti–mouse ATAD2 cs50563 1/500 (Cell Signaling Technology), anti–MYC ab32072 1/1,000 (Abcam, RRID: AB_731658), anti–β-actin cs4970 1/20,000 (Cell Signaling Technology, RRID: AB_2223172), and anti–GAPDH cs5174 1/1,000 (Cell Signaling Technology, RRID: AB_10622025), and secondary antibodies (anti–rabbit IgG HRP Sigma NA934 1/10,000, RRID: AB_2722659) and visualized using an ECL Plus Western Blotting Detection Kit (Thermo Fisher Scientific RPN2232). X-ray films were developed and scanned, or membranes were scanned with an iBright 1500 imager (Invitrogen). Band intensities were quantified relative to β-actin or GAPDH using ImageJ 1.54g software (RRID: SCR_003070).

Description of human patient cohorts and datasets

All patients consented before inclusion, and all studies using human tissue specimens were performed according to protocols approved by the Human Research Protection Office and Institutional Review Board at Columbia University Irving Medical Center

(CUIMC). Only male patients were involved as the focus of our study was prostate cancer. Anonymized human tissue specimens were obtained from the CUIMC cohort Molecular Pathology Shared Resource of the Herbert Irving Comprehensive Cancer Center (HICCC) as two sets of samples from independent patients. The first set (15, 17) consisted of 5 bone metastatic resections and 10 primary prostate cancer tumors (Gleason score 9) from surgical resections of patients with advanced prostate cancer that were used for RNA isolation and qPCR studies. The second set consisted of 10 radical prostatectomy samples and 4 bone metastasis biopsies from patients with prostate cancer, used for IHC studies. RNA was extracted using the miRNeasy Mini Kit (QIAGEN), and RT-qPCR was performed using the QuantiTect SYBR Green PCR kit (QIAGEN).

Analysis of ATAD2 expression in human prostate cancer tumors and metastases were also performed by staining of two independent tissue microarrays (TMA). These studies were approved by the Institutional Review Board of Memorial Sloan Kettering Cancer Center or University of Michigan. The HICCC TMA was previously described (39) and consisted of 338 samples that were stained and scored. These included 110 benign tissues and primary tumors of Gleason scores 6 ($n = 111$), 7 ($n = 69$), 8 ($n = 30$), and 9 ($n = 18$). The University of Washington (UW) TMA was obtained through the Prostate Cancer Biorepository Network and consisted of 51 bone and 70 visceral metastases obtained from 45 patients at rapid autopsy at the UW. A total of 50 bone and 65 visceral samples were successfully stained and scored, each represented by three cores, and the average of the three cores was considered for every sample. Immunostaining was quantified by the percentage of positively stained nuclei.

Two independent cohorts with clinical outcome data retrieved from the Decipher GRID registry, the Mayo cohort, GSE62116 (40), and the Johns Hopkins Medical Institute (JHMI) cohort, GSE79957 (41), were used for metastasis-free survival analyses. Patients in the Mayo cohort ($n = 235$) had undergone radical prostatectomy between 2000 and 2006; the median follow-up was 7 years with 73 patients developing metastasis. The JHMI cohort is a case cohort of 260 men who had undergone radical prostatectomy between 1992 and 2010 at intermediate or high risk and received no additional treatment until the time of metastasis; the median follow-up was 9 years with 99 patients developing metastasis. Both cohorts were profiled on a Human Exon 1.0 ST Array, and hybridization was conducted in a Clinical Laboratory Improvement Amendments–certified laboratory facility (Veracyte Inc.). For comparison of ATAD2 mRNA expression in primary and metastatic prostate cancer, normalized microarray expression values were downloaded from Gene Expression Omnibus [GSE35988 (42) and GSE3325 (43)] and analyzed with the two-tailed t test.

Correlation of ATAD2 expression and MYC signaling was performed using data downloaded directly from cBioPortal (44) using The Cancer Genome Atlas firehose legacy ($n = 491$ primary tumors; ref. 45), SU2C/PCF dream team [SU2C (46) polyA cohort, $n = 266$ metastases], and Fred Hutchinson Cancer Research Center (FHCRC) ($n = 149$ metastases; ref. 47) datasets. Z-score sums from genes in the Myc Hallmarks v1 gene set from MSigDB (https://www.gsea-msigdb.org/gsea/msigdb) were used to estimate MYC pathway levels.

Lentivirus production and transduction

HEK-293FT cells were plated at ~90% confluency into 150-mm dishes 24 hours before transfection, in DMEM-10% FBS culture media. A measure of 30 μg of lentiviral vector (Sigma-Aldrich) along with 24-μg psPAX2 (Addgene, RRID: Addgene_12260) and 12 μg pMD2.G (RRID: Addgene_12259) packaging plasmids were diluted in Opti-MEM I media (Thermo Fisher Scientific) and mixed with 60 μg/mL polyethylenimine (Sigma-Aldrich) for transfection into HEK-293FT cells. After overnight incubation, the media were replaced with DMEM-1% FBS for 48 hours, centrifuged at 300 *g* for 5 minutes, and filtered through a 0.45-μm filter to obtain the virus supernatant that was mixed with 0.8 μg/mL polybrene (Sigma-Aldrich) to infect target cells. Tissue culture media were changed 48 hours after viral infection and supplemented with 2 μg/mL puromycin for 72 hours. short hairpin RNA (shRNA) vectors used were pLKO.1 (Sigma-Aldrich) nontargeting control SHC002, shMYC#1 TRCN0000039640, shMYC#2 TRCN0000039642, shATAD2#1 TRCN0000161812, shATAD2#2 TRCN0000159158, shATAD2#3 TRCN0000158789, and shAtad2 (mouse) TRCN0000098627. CRISPRa was performed in 22Rv1 cells, as previously described (17), using pHRdSV40-dCas9-10xGCN4_v4-P2A-BFP (RRID: Addgene_60903) and pHRdSV40-scFv-GCN4-sfGFP-VP64-GB1-NLS (RRID: Addgene_60904) plasmids to derive clonal derivatives showing high and homogenous levels of gene activation. single-guide RNA (sgRNA) sequences targeting ATAD2 (or nontargeting controls) were cloned into BstXI- and BlpI (New England Biolabs)-digested pU6-sgRNA EF1Alpha-puro-T2A-BFP vector (RRID: Addgene_60955) by oligonucleotide annealing and ligation, as previously described (17). Sequences of all sgRNAs used in this study are provided in Supplementary Table S2.

Colony formation assays

A total of 1,000 human or 200 mouse cells were plated in triplicate in six-well plates and allowed to grow for 2 weeks before fixation in 10% formalin and stained with 0.5% crystal violet. Colonies were quantified with ImageJ software (https://imagej.nih.gov/ij/) using the "Analyze particle" tool with size 50 infinity and circularity 0.4 to 1.0. Assays were performed with a minimum of two independent biological replicates.

Intratibial and intracardiac implantation studies

For monitoring tumor growth in bone, PC-3 cells (1×10^6 cells in 10 μL of PBS) were injected into the tibiae of male NOD/SCID mice. A small longitudinal skin incision was made across the knee capsule, the tip of a scalpel was used to drill a hole into which cells were injected, sterile surgical bone wax (CP Medical) was used to seal the hole, and the skin was then closed with wound clips. Tumor growth was monitored biweekly by bioluminescence imaging using an IVIS Spectrum Optical Imaging System (PerkinElmer), following an intraperitoneal injection of 150 mg/kg D-luciferin (PerkinElmer). Images were quantified using Living Image Software (PerkinElmer).

For intracardiac metastasis assays, mouse *NPK* bone metastatic cells (1×10^5 cells in 100 μL of PBS; ref. 15) were injected percutaneously into the left heart ventricle of nude mice (male, Taconic) and mice were euthanized 12 to 14 days after injection. At the time of sacrifice, yellow fluorescent protein-positive tumors and metastases were visualized by *ex vivo* fluorescence using an Olympus SZX16 microscope (Ex 490–500/Em 510–560 filter).

Organ-on-a-chip invasion assay

Engineered bone tissues were made from bovine calf metacarpals (Lampire Biological Laboratories, 19D24003) that were sectioned into rectangular scaffolds (4 mm wide × 8 mm long × 1 mm thick) and fully decellularized, as detailed previously (48, 49). The decellularization process removed all bovine cellular components, leaving

just the bone extracellular matrix and bone architecture. The bones were lyophilized, and the only bone scaffolds weighing between 12 and 18 mg/scaffold were included, resulting in the starting material with uniform porosity for engineering bone tissue. After sterilization in 70% ethanol overnight and 24 hours of incubation in DMEM, the bone scaffolds were seeded with human cells.

Human bone marrow–derived mesenchymal stem cells (MSC; Lonza) were infused into the bone scaffolds (4×10^5 cells per scaffold) by suspending the cells in 40 μL of medium [DMEM supplemented with 10% (v/v) HyClone FBS, 1% penicillin/streptomycin, and 1 ng/mL of basic FGF] and letting the cells attach for 2 hours before adding additional media (2 mL per well). To support the differentiation of the MSCs into osteoblasts within the engineered bone matrix, the MSC-seeded bone was cultured in osteogenic medium consisting of low-glucose DMEM supplemented with 1 μmol/L dexamethasone (Sigma-Aldrich), 10 mmol/L β-glycerophosphate (Sigma-Aldrich), and 50 μmol/L L-ascorbic acid 2-phosphate (Sigma-Aldrich).

The osteogenic differentiation process continued for 3 weeks, with media changes three times a week. To create osteolytic bone, we then infused primary monocytes into the osteoblastic bone scaffolds (49). $CD14^+$ monocytes were obtained by negative selection (EasySep Human Monocyte Isolation Kit, STEMCELL Technologies, 19359) from peripheral blood mononuclear cells isolated from buffy coats of human blood (fully deidentified samples obtained from the New York Blood Center) via density gradient centrifugation with Ficoll-Paque PLUS (GE HealthCare, 17-1440-02). Purified monocytes were seeded into the engineered bone tissues (4×10^5 cells per scaffold) by suspending the cells in 40 μL of osteolytic medium for 2 hours. The engineered bone tissues were then cultured for a week in 2 mL of osteolytic media [Eagle Minimum Essential Medium Alpha modification (Sigma, M4526) supplemented with 10% (v/v) heat-inactivated HyClone FBS, 1% penicillin/streptomycin, L-glutamine (Gibco, 25030-081), 20 ng mL^{-1} Recombinant Human M-CSF (PeproTech, 300-25), and 40 ng mL^{-1} Recombinant Human sRANK Ligand (PeproTech, 310-01)], with media changes and fresh cytokines every 3 days.

The engineered bone tissues were then placed into a chip designed for interorgan communication that we recently developed (48). In brief, engineered vascular barriers are formed by seeding 1.5×10^5 MSCs and 4×10^5 human umbilical venous endothelial cells on custom-made transwell inserts. After the cells attached to the transwell barrier and formed a confluent monolayer, they were placed into the one-tissue multi-organ chip and exposed to increasing levels of shear stress (0.31 dynes cm^{-2} for 12 hours, 0.63 dynes cm^{-2} for 24 hours, and 1.88 dynes cm^{-2} for 24 hours). The ramping of shear creates a confluent and quiescent vascular barrier lining the bottom of the chamber with engineered bone. After the engineered bone is added to the chamber (directly above the vascular barrier), circulating primary tumor cells were introduced into the vascular reservoir and allowed to circulate underneath the vascular barrier at a hydrodynamic shear stress of 1.88 dynes cm^{-2}.

The cancer cells were labeled (LuminiCell Tracker 670, Sigma-Aldrich) to enable downstream tracking and allowed to circulate for 4 weeks. Media changes occurred every other day by replacing 1 mL of medium from the vascular reservoir with fresh vascular medium (EGM-2, Lonza) and 1 mL of medium from the engineered bone tissue reservoir with the osteolytic medium specified above.

Intravasation of circulating cancer cells within the bone tissues was tracked using the IVIS Spectrum Optical Imaging System (PerkinElmer) in Columbia University's Oncology Precision Therapeutics and Imaging Core. The chips with engineered tissues were placed next to one another in the same field of view and imaged using an IVIS 200 Spectrum device. The corresponding IVIS Spectrum software application (PerkinElmer) was used to analyze the images by converting the signal to the normalized radiant efficiency [emission light (photons/seconds.cm^2 str)/excitation light (μW/cm^2)]. We measured the fluorescence of the labeled cancer cells within the engineered bone tissues by selecting the same region of interest for each tissue and quantifying the sum of the radiant efficiency of all fluorescent pixels within the region of interest.

Statistical analyses

The Fisher exact test was used to compare two groups of categorical data; a two-tailed *t* test or one-way ANOVA (with Dunnett multiple comparisons) was used to compare two or more groups of numerical data after testing for normal distribution using D'Agostino–Pearson or Kolmogorov–Smirnov tests. Nonparametric tests were used if a normal distribution test was not passed, as stated in the figure legends. Kaplan–Meier survival analysis was conducted using GraphPad Prism software and analyzed with the log-rank test. Correlation studies were performed with the Spearman test using a two-tailed *P* value. For all box plots, boxes show the 25th to 75th percentile, center lines show the median, and whiskers show the minimum–maximum values. In all bar graphs and dotplots, means are represented and error bars show the SD. GraphPad Prism software (v.10.0; RRID: SCR_002798) was used for statistical calculations and data visualization. BioRender license was issued to the Department of Oncological Sciences at Mount Sinai School of Medicine.

Data availability

The data generated in this study are available within the article and its supplementary data files. Expression profile data analyzed in this study were obtained from Gene Expression Omnibus at GSE35988, GSE3325, GSE62116, GSE79957, GSE178869, and GSE117430 or using cBioPortal (44).

Results

ATAD2 is progressively expressed in metastatic prostate cancer

We first evaluated ATAD2 expression in primary tumors from different prostate cancer GEMMs of varying metastatic potential, in which tumors are induced in luminal cells of the adult mouse prostate by virtue of the *Nkx3-1*^{CreERT2} allele (50). IHC staining of indolent tumors (from *Nkx3-1*^{CreERT2}; *Pten*$^{flox/flox}$, termed "*NP*" mice) showed low levels of nuclear ATAD2 staining (mean = 4.9% and $n = 6$), as shown in **Fig. 1A** and Supplementary Table S1. In contrast, tumors from highly metastatic "*NPK*" (*NP-Kras*$^{LSL-G12D}$) mouse models (that include ~45% penetrance to bone; ref. 15) showed significantly higher levels of ATAD2 expression in both primary tumors (mean = 34.3%, $n = 9$, $P = 0.0002$) and unmatched metastases (mean = 36.1%, $n = 5$, $P = 0.0006$). Interestingly, when *NPK* tumors were examined early during prostate cancer progression ("early prostate" in **Fig. 1A**, i.e., 1–2 months after tumor induction; ref. 16) before any evidence of established metastasis, ATAD2 expression was low as in indolent tumors (mean = 4.6%, $n = 4$). This upregulation of ATAD2 expression upon progression of this highly metastatic model coincides with histologic transition to carcinoma and with MYC overexpression (previously reported in

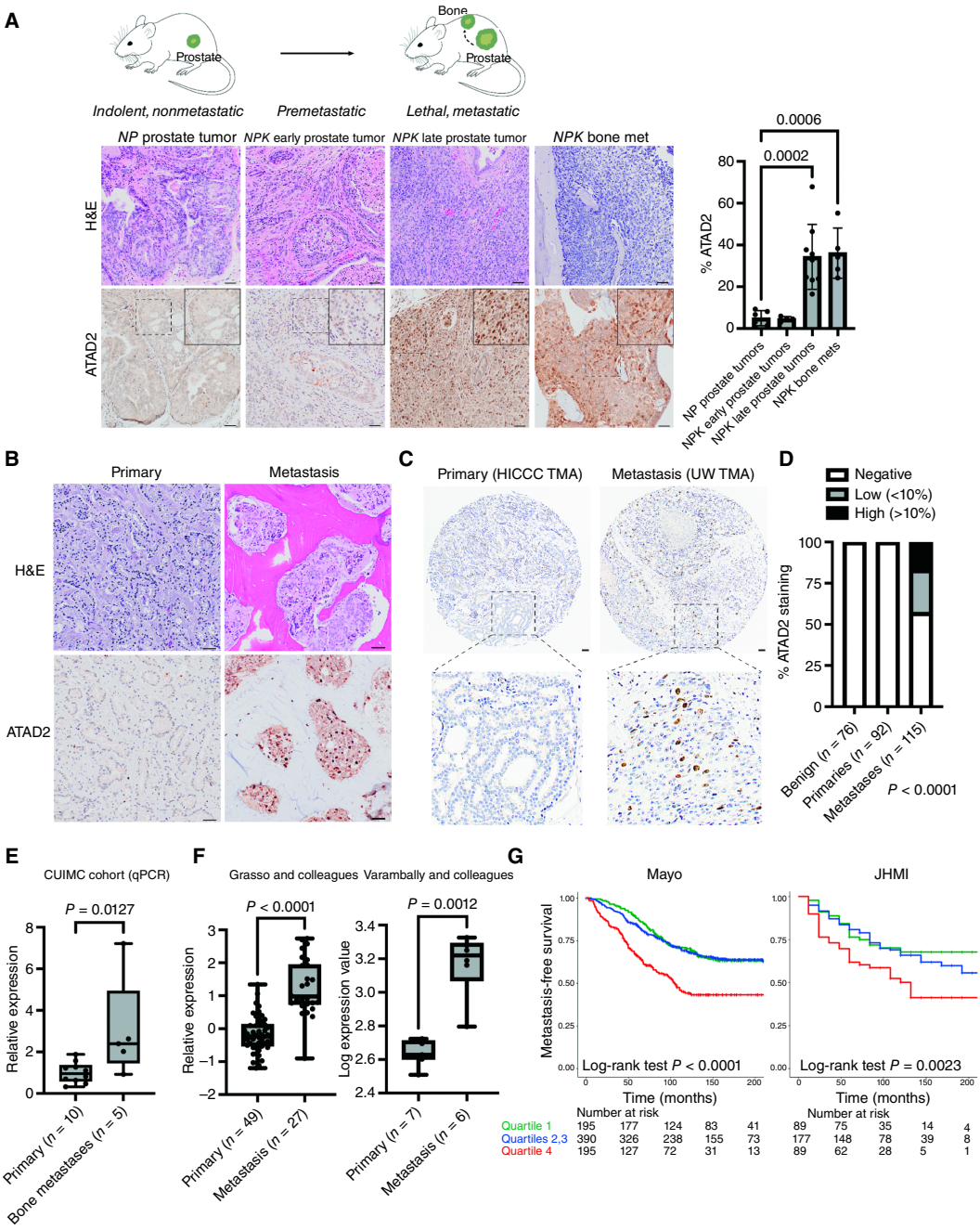

Figure 1.

ATAD2 is expressed in human and mouse metastatic prostate cancer and associated with the development of metastasis. **A,** Schematic diagrams of different GEMMs that recapitulate the progression of prostate cancer (green) from indolent (nonlethal) *NP* tumors, early premetastatic *NPK* tumors (i.e., before development of metastasis), and late, highly metastatic tumors that include metastasis to bone. Representative histologic sections stained by H&E and IHC for ATAD2 are shown, including a bone metastasis from a late *NPK* mouse. The region delimited by boxes is amplified in the inset to show nuclear staining. Scatter plots show the quantification of ATAD2 nuclear positivity in tumors from each category, with *P* values from one-way ANOVA with Dunnett multiple comparisons test compared with NP. **B,** Representative histologic sections stained by H&E and IHC for ATAD2 on whole-tissue primary tumors obtained from radical prostatectomies, as well as metastases from bone biopsies. **C,** ATAD2 IHC on TMA cores from a representative negative primary tumor and a metastasis with high ATAD2 expression. The region delimited by boxes is amplified to show nuclear staining. **D,** Stacked bar graphs showing quantification of ATAD2 positivity in different TMA tissues. The *P* value shown is for the Fisher exact test comparing ATAD2 positivity (using a 1% expression cutoff) in primaries vs. metastases. **E** and **F,** Box plots showing relative expression of ATAD2 in primary tumors and metastasis from three different patient cohorts. **E,** CUIMC cohort analyzed by qRT-PCR. **F,** Publicly available datasets from microarray expression data. *P* values in **E** and **F** are for an unpaired, double-sided *t* test. **G,** Kaplan–Meier metastasis-free survival curves of ATAD2 expression stratified by quartiles in the Mayo (left) and JHMI (right) cohorts of primary tumors with prolonged follow-up data. *P* values were estimated using a log-rank test. Scale bars, 50 μm. H&E, hematoxylin and eosin; met, metastases. (**A,** Created with BioRender.com.)

ref. 15), as illustrated in Supplementary Fig. S1A. Thus, the correlation of ATAD2 expression with metastatic propensity in different prostate cancer GEMMs suggests that ATAD2 may play a functional role in the development of metastasis.

We next examined the protein expression of ATAD2 in clinical specimens by IHC in several patient cohorts. Using whole-tissue sections from 10 radical prostatectomies and four bone biopsies obtained at CUIMC, we observed nuclear ATAD2 staining to be mostly negative in primary tumors (<0.1% positivity). In contrast, three of four bone metastases showed strong and high (>10%) nuclear positivity in tumor cells (**Fig. 1B**). We used TMAs to quantify ATAD2 expression in tissues spanning the progression of prostate cancer, as shown in **Fig. 1C**. This included the "HICCC TMA" (39) containing 76 benign tissue samples (with 110 cores) and 92 primary tumors (with 228 cores and Gleason scores 6–9), as well as the "UW TMA" containing 115 metastases from 45 patients in a rapid autopsy program at the UW (containing three cores each of 50 bone and 65 visceral metastases). **Table 1** summarizes the histoclinical characteristics of these samples. Strikingly, ATAD2 staining was negative in all 338 localized (benign and malignant) samples, whereas more than a third of metastases (37%, 43/115) showed strong nuclear positivity in at least 1% of cells, thus confirming a significant enrichment in expression in metastases compared with localized tumors ($P < 0.0001$, Fisher exact two-tailed test, **Fig. 1D**). Additional IHC images representative of different ATAD2 positivity scores are shown in Supplementary Fig. S1B–S1D. Of note, we did not detect differences in expression between different metastatic sites, or association with survival outcomes or response to the standard of care treatments (androgen deprivation, enzalutamide or abiraterone), as shown in Supplementary Fig. S1E.

To evaluate the expression of *ATAD2* mRNA in human prostate cancer, we performed qPCR analysis of a patient cohort using RNA extractions from 10 primary tumors and five bone metastases (CUIMC cohort, independent from samples used for IHC analysis), as well as analysis of two publicly available datasets (42, 43). These findings showed that *ATAD2* mRNA levels were significantly enriched in metastases in all of these cohorts [$P = 0.0127$ for CUIMC, $P < 0.0001$ for GSE35988, Grasso and colleagues (42), and $P = 0.0012$ for GSE3325, Varambally and colleagues (43), **Fig. 1E** and **F**].

To assess whether *ATAD2* is significantly associated with the risk of metastasis, we used two independent prostatectomy cohorts with extensive clinical outcome data [Mayo (40) and JHMI (41); **Fig. 1G**]. Patients in Mayo ($n = 235$) had undergone radical prostatectomy between 2000 and 2006 with a median follow-up of 7 years during which time 76 patients developed metastasis. Patients in JHMI ($n = 260$) had undergone radical prostatectomy between 1992 and 2010 with a median follow-up of 9 years, and 99 patients developed metastasis. Indeed, patients with tumors that scored in the 4th quartile of *ATAD2* expression (i.e., the top 25%) showed a significantly worse metastasis-free survival compared with the rest of the patients ($P < 0.0001$ and $P = 0.0023$ for Mayo and JHMI, respectively, **Fig. 1G**). Overall, ATAD2 expression in patients with prostate cancer is overexpressed in metastases compared with primary tumors, and expression in primary tumors is significantly associated with metastasis survival.

ATAD2 expression may be regulated by MYC

MYC signaling is among the most commonly activated pathways in bone metastasis compared with primary tumors in both the *NPK* model (15) as well as in human tumors (15, 37). Both ATAD2 and MYC reside near each other in a chromosomal location that is frequently amplified in prostate and other cancers. Moreover, ATAD2 has been previously shown to interact with MYC and modulate its transcriptional activity (31). We thus studied the relationship between *ATAD2* expression and MYC pathway activation in several human datasets using cBioPortal (44). *ATAD2* expression was positively and significantly correlated with MYC pathway signaling in metastases from two datasets, SU2C (Spearman $R = 0.4072$, $P < 0.0001$, $n = 266$; ref. 46) and FHCRC ($R = 0.4810$, $P < 0.0001$, $n = 149$; ref. 47) but not in primary tumors from The Cancer Genome Atlas ($n = 491$; **Fig. 2A** and **B**). Stratification of the latter cohort into quartiles showed that only the fourth quartile of *ATAD2* expression was positively and significantly correlated with MYC pathway signaling [$R = 0.3982$, $P < 0.0001$, **Fig. 2A** (right)], consistent with our previous results showing that high expression in primary tumors is associated with the development of metastasis (**Fig. 1G**). This suggests that MYC activation may lead to ATAD2 expression in metastatic castration-resistant prostate cancer. In support of this, using publicly available datasets from ENCODE (51), we show that the promoter of ATAD2 and an upstream cis-regulatory region are both enriched for the H3K27Ac histone mark, suggestive of active promoters/enhancer regions, and bound by MYC in prostate cancer cell lines [22Rv1 (52) and LNCaP (53), **Fig. 2C**].

To functionally validate whether MYC regulates the expression of ATAD2, we used two shRNAs to knockdown MYC in four human prostate cancer cell lines. This resulted in downregulation of ATAD2 protein and mRNA levels in LNCaP and PC-3 cells (including well-known MYC targets, **Fig. 2D** and **E**) but not in 22Rv1 and DU145 cells (Supplementary Fig. S2A), suggesting that MYC may indeed regulate the expression of ATAD2 in a subset, but not all, of prostate tumors.

ATAD2 inhibition affects prostate cancer proliferation and metastasis

Having established that ATAD2 is overexpressed in advanced stages of prostate cancer, we set out to determine whether it would serve as a valid therapeutic target to diminish prostate cancer growth and metastasis. We first performed shRNA-mediated knockdown of ATAD2 to study its effects on tumor proliferation. Knockdown of ATAD2 using three shRNAs significantly impaired cell proliferation in four human prostate cancer cell lines compared with shControl, irrespective of AR status, including AR-positive androgen-dependent LNCaP cells, AR-positive androgen-independent 22Rv1 cells, as well as AR-negative PC-3 and DU145 cells, as measured by colony formation assays ($P < 0.0001$ one-way ANOVA with Dunnett multiple comparisons test, $n = 3$ technical replicates; **Fig. 3A**; Supplementary Fig. S3A). Next, we selected PC-3 cells because of their well-studied growth in bone and labeled them with GFP and luciferase to facilitate *in vivo* tracking of tumor growth. We then injected shControl- and shATAD2-treated cells into the bones (tibiae) of immunodeficient SCID mice to study tumor growth in bone. We chose shATAD2#2 as it shows modest effects on *in vitro* proliferation (**Fig. 3A**), allowing us to collect enough cells for *in vivo* injection. Notably, knockdown of ATAD2 resulted in slower tumor growth in bones of mice compared with shControl (**Fig. 3B**), as measured by longitudinal luciferase tracking ($P = 0.0023$, two-way ANOVA with Šídák multiple comparisons test to day 22, two replicate experiments, $n = 5$ mice each), suggesting that ATAD2 inhibition may be a viable therapeutic strategy to impair tumor growth in bones.

Table 1. Characteristics of patients in TMA cohorts.

TMA:	HICCC	UW			
Clinical parameter	**All patients (*n* = 92)**	**All patients (*n* = 45)**	**ATAD2-negative (*n* = 25)**	**ATAD2-positive (*n* = 20)**	***P* value**
Gleason score no. (%)	of tissue cores[a] (*n* = 228)	of primary tissue at diagnosis[b]			
6	111 (49)	2 (5)	0 (0)	2 (11)	0.5307[c]
7	69 (30)	16 (37)	9 (38)	7 (37)	
8	30 (13)	7 (16)	4 (17)	3 (16)	
9–10	18 (8)	18 (42)	11 (46)	7 (37)	
PSA at diagnosis (ng/mL; median, range)	8.1 (0–118)	11.3 (0.68–1,316)	17.4 (0.68–701)	9 (4.4–1,316)	0.2955[d]
Age at diagnosis (years; median, range)	61 (40–74)	63 (43–77)	63 (43–77)	63 (45–75)	0.9026[e]

[a]Malignant tissue cores at radical prostatectomy.
[b]Gleason score information was missing for two patients.
[c]Two-sided Fisher exact test comparing Gleason scores ≤7 vs. > 8.
[d]Two-tailed Mann–Whitney U test.
[e]Two-tailed *t* test.

Histologic analysis of the tumor lesions in bone confirmed sustained ATAD2 knockdown in shATAD2-treated tumors compared with shControl ($P = 0.0081$ by two-tailed t test, $n = 3$ tumors, **Fig. 3C**). Interestingly, we also observed significant downregulation of MYC expression in shATAD2 intratibial xenografts ($P = 0.0001$ by two-tailed t test, $n = 3$, **Fig. 3C**), suggesting that ATAD2 may, in turn, regulate MYC expression. We thus measured MYC expression and three well-known MYC targets in LNCaP and PC-3 cells treated *in vitro* with shATAD2. Although this resulted in a significant downregulation of MYC expression (Supplementary Fig. S3B) and of its downstream targets (Supplementary Fig. S3C) in LNCaP cells, loss of ATAD2 did not show evidence of diminishing MYC levels or transcriptional activity in PC-3 cells, showing discrepancies between the *in vivo* and *in vitro* effects in this cell line that would be interesting to understand in future studies.

Given its significant association with metastasis in human prostate cancer specimens, we next examined whether ATAD2 could play a functional role in the development of bone metastasis. First, we used state-of-the-art engineered human tissue-on-a-chip to model invasion of tumor cells across a vascular barrier and into an engineered bone (**Fig. 4A** and **B**). As we have previously described (17, 48), tumor cells are introduced into a circulating flow that is separated by a vascular barrier from a chamber containing engineered bone. Cells are cultured in this way for 4 weeks, allowed to migrate through the endothelial lining into the bone chamber, and the resulting invading cells are quantified by fluorescence emission (**Fig. 4A**). We first knocked down Atad2 in our highly bone metastatic *NPK* cell lines and assessed the effects on invasion into engineered bone. Compared with nonmetastatic *NP* cells (15), which express low levels of ATAD2 (**Fig. 4B**), *NPK* cell lines showed a significant increase in invasion to bone, which was completely abolished by knockdown of Atad2, resulting in comparable invasion to *NP* cells ($P < 0.0001$ for *NP* and shAtad2, one-way ANOVA with Dunnett multiple comparisons test to *NPK* shControl, $n = 3$; **Fig. 4B**).

We also used CRISPRa (ref. 54) to overexpress ATAD2 from its endogenous locus in 22Rv1 cells and observed a significant increase in invasion to bone using two independent sgRNAs targeting ATAD2, compared with nontargeting sgControl cells ($P = 0.004$ for sgATAD2#1 and $P = 0.0006$ for sgATAD2#2, one-way ANOVA with Dunnett multiple comparisons test, $n = 3$; Supplementary Fig. S4A).

In contrast with knockdown in *NP* cell lines (Supplementary Fig. S4B), shAtad2 treatment in *NPK* cells resulted in reduced proliferation rates *in vitro* ($P < 0.0001$, two-tailed test compared with shControl, Supplementary Fig. S4C). Moreover, this markedly reduced MYC protein levels ($P = 0.0279$, two-tailed t test, Supplementary Fig. S4D), supporting our hypothesis that ATAD2 may regulate MYC expression at least in certain tumors.

In order to directly assess the effect of ATAD2 on metastasis, we treated our highly bone metastatic *NPK* cells with shControl or shATAD2 for 5 days and then performed experimental metastasis assays using intracardiac injections into the circulation of immunodeficient *nude* mice. Remarkably, ATAD2 knockdown in *NPK* tumors resulted in a significant reduction in the number of ensuing bone and liver metastases (**Fig. 4C**, $P = 0.0024$ for bone and $P = 0.0277$ for liver metastases, two-tailed t test, $n = 23$ in three replicate experiments), establishing ATAD2 as a driver of prostate cancer metastasis. Representative epifluorescence images of bones and livers, as well as histologic confirmation of bone metastasis by hematoxylin and eosin and IHC for YFP and ATAD2, are shown in **Fig. 4C**. Of note, despite potent knockdown in shAtad2 (**Fig. 4B**; Supplementary Fig. S4D), 50% (three of six) of histologically examined bone metastases expressed high levels of ATAD2 comparable with shControls (Supplementary Fig. S4E), implying that a subset of shAtad2 tumors has either escaped knockdown or regained ATAD2 expression, further supporting a role for ATAD2 in bone metastasis.

Discussion

The occurrence of metastasis is a crucial determinant of prognosis in prostate cancer as well as in many other solid tumors (1). Defining the molecular principles of this process is therefore an urgent unmet need that may have critical translational implications for the development of novel therapies and biomarkers. In this study, we have leveraged mouse models of spontaneous prostate cancer progression to bone metastasis, as well as multiple independent patient cohorts to establish a functional role for ATAD2 in metastasis. We have focused on bone, the most clinically relevant

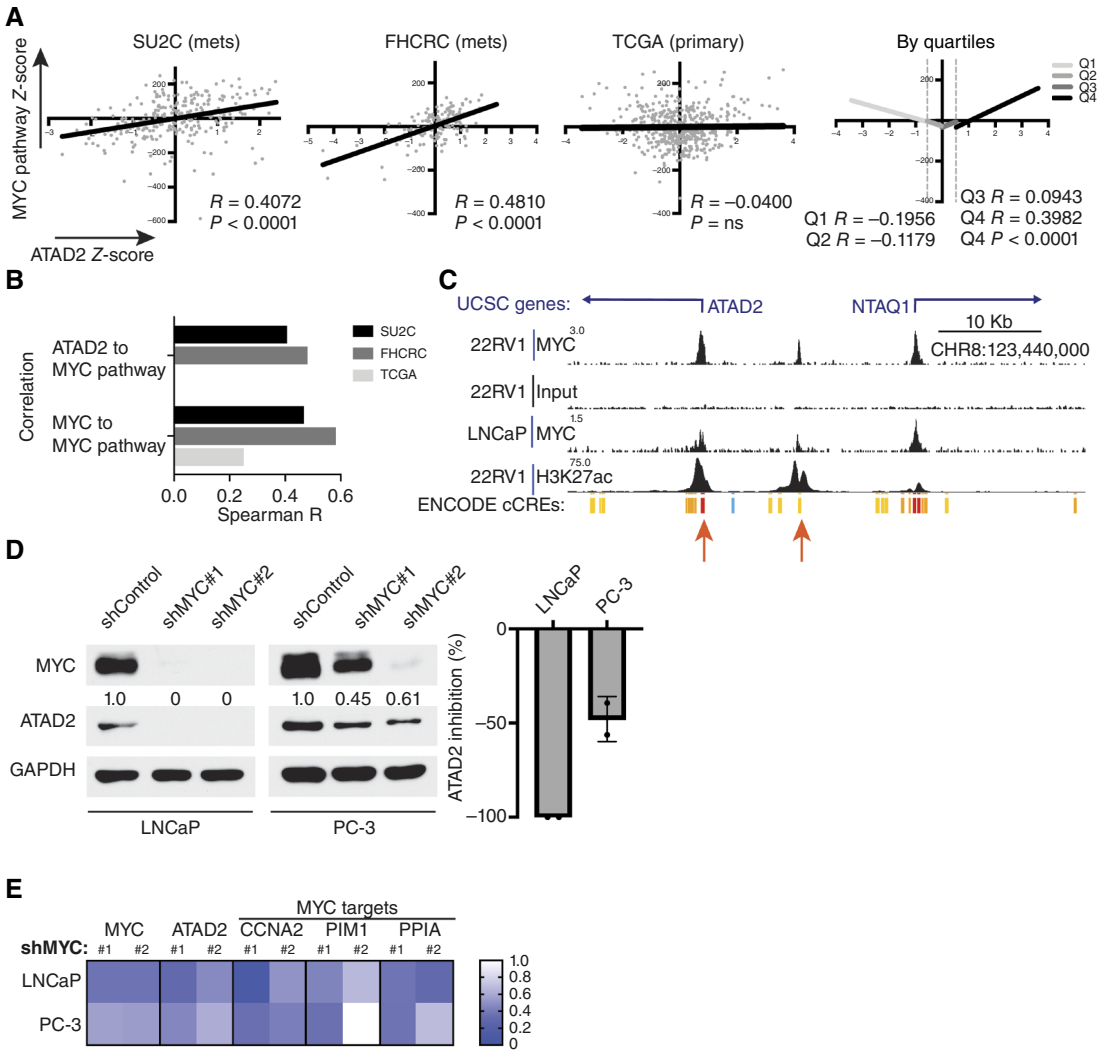

Figure 2.

Association between MYC and ATAD2 expression. **A,** Correlation between ATAD2 expression and MYC pathway activation in two metastatic (SU2C, $n = 266$ and FHCRC, $n = 149$) and one primary (TCGA, $n = 491$) prostate cancer patient cohorts. MYC pathway activity was estimated based on the sum of *Z*-scores from genes in the MYC Hallmarks v1 gene set of MYC targets. R and *P* values are derived from the Spearman test, and the linear regression line is shown. The fourth graph on the right depicts linear regression lines on the TCGA cohort subdivided by quartiles (Q1–Q4) of ATAD2 expression, and R values are shown below for each quartile. **B,** Bar graph summarizing correlations between ATAD2 and MYC mRNA with the MYC pathway in the three datasets. Only significant correlations ($P < 0.01$) are shown. **C,** Capture of the UCSC genome browser (GRCh33/hg38) showing ~60 kb region on human chromosome 8 around *ATAD2* promoter (*y* axis = reads per kilobase per million reads). UCSC genes (blue) at the top. Putative ENCODE candidate cis-regulatory elements (cCRE) are shown at the bottom, with color codes according to ENCODE classification of regulatory signatures: red = promoter-like, orange = proximal enhancer–like, and yellow = distal enhancer–like. Embedded chromatin immunoprecipitation sequencing (ChIP-seq) tracks were obtained from Holmes and colleagues for 22Rv1 (H3K27ac, MYC, and input) and from Augello and colleagues for LNCaP (MYC) cell lines. Orange arrows point to two putative MYC regulatory elements in the ATAD2 promoter region. **D,** Western blot analysis of ATAD2 expression upon MYC knockdown in human LNCaP and PC-3 cells. The numbers on top of the ATAD2 bands show their expression relative to shControl and are summarized as % inhibition in scatter plots on the right. **E,** Heatmap summarizing qRT-PCR analysis of MYC, ATAD2, and three well-known MYC targets after MYC knockdown in LNCaP and PC-3 cells. Color scale depicts fold change downregulation compared with shControl. Only significant changes are colored ($P < 0.05$ using one-way ANOVA adjusted for multiple comparisons with the Dunnett test compared with shControl). met, metastases; ns, nonsignificant; TCGA, The Cancer Genome Atlas.

metastatic site in prostate cancer, by leveraging unique mouse models and state-of-the-art tissue engineering technologies.

Our work shows that ATAD2 is overexpressed in advanced stages of prostate cancer progression and identifies MYC as a critical regulator of its expression in a subset of tumors. Because MYC overexpression may occur in early primary tumors (36) before ATAD2 expression is evident, other mechanisms may cooperate with MYC to drive ATAD2 expression in advanced tumors, including previously reported AR and E2F transcription factors (32, 33). One potential mechanism is coamplification of both the *MYC* and *ATAD2* genomic loci, given their proximity in chromosome 8q, a region frequently amplified in later stages of progression (46).

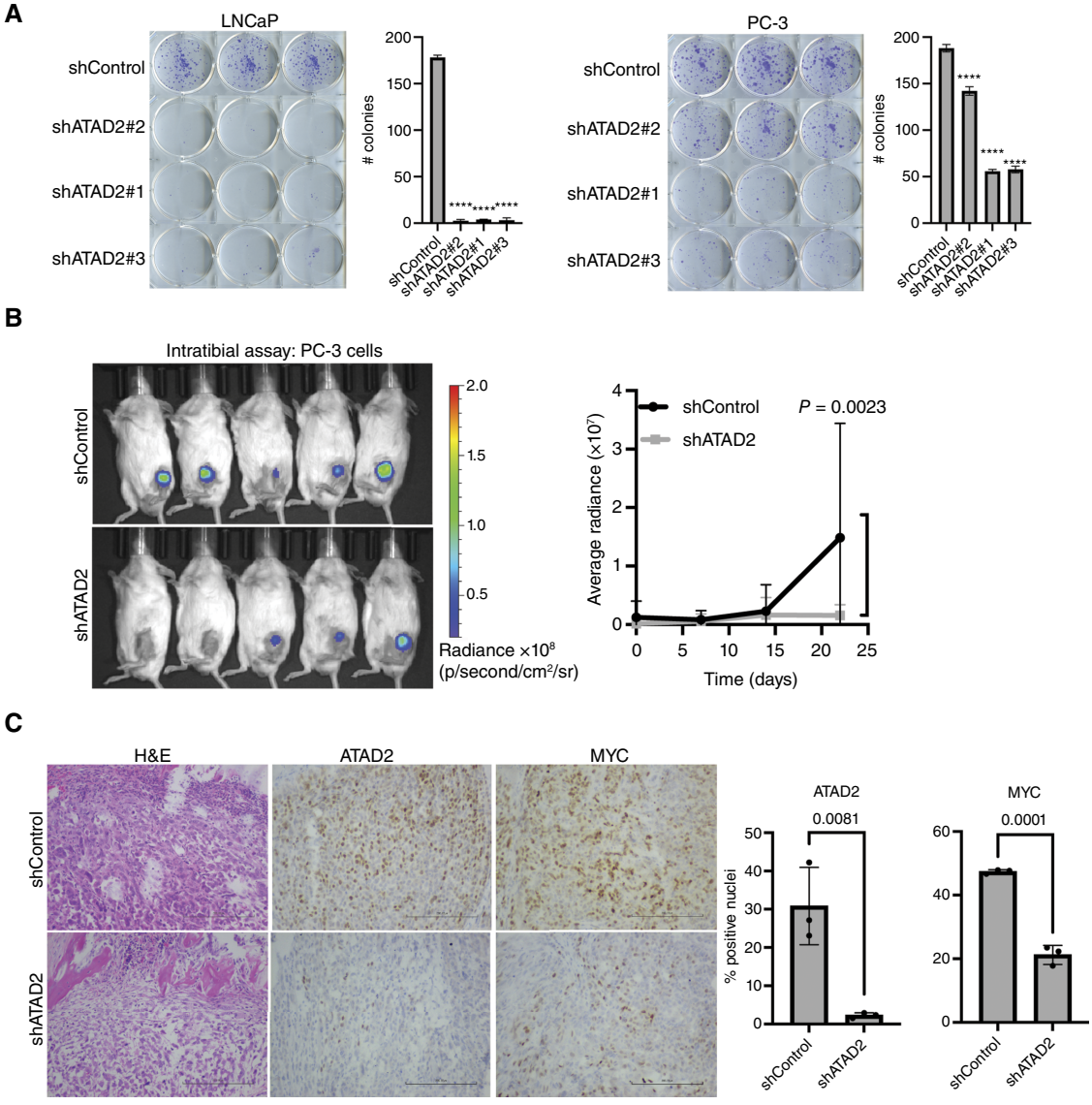

Figure 3.

ATAD2 knockdown impairs proliferation of prostate cancer cells. **A,** Colony formation assays of LNCaP and PC-3 human cell lines after knockdown of ATAD2, stained with crystal violet. Asterisks denote *P* values from one-way ANOVA with Dunnett multiple comparisons test, $n = 3$ technical replicates. ****, $P < 0.0001$. **B,** Intratibial growth assays of PC-3 cells labeled with GFP-luciferase (two replicate experiments, $n = 5$ each). Representative IVIS bioluminescence images of shControl and shATAD2 tumors after intratibial injection, along with tumor growth curves quantified by longitudinal bioluminescence imaging. *P* value shown for day 22 was estimated by two-way ANOVA with Šídák multiple comparisons against shControl. **C,** Representative H&E, ATAD2, and MYC IHC staining of intratibial PC-3 grafts treated with shControl or shATAD2. Scale bars, 200 μm. Scatter plots on the right show quantification of percent tumor nuclei positive for ATAD2 or MYC, with *P* values derived from the two-tailed unpaired *t* test and $n = 3$. H&E, hematoxylin and eosin.

We further show that genetic downregulation of ATAD2 diminishes proliferation and metastasis in advanced prostate tumors, thus establishing ATAD2 as a promising therapeutic target for advanced disease. Future studies should address the feasibility of achieving this, for example, through recently developed small-molecule inhibitors that specifically bind the ATAD2 bromodomain (55–58). We note that although our shRNA studies show that ATAD2 affects tumor proliferation in multiple prostate cancer cell lines, LNCaP cells are particularly sensitive to this inhibition. Given that shATAD2 causes a strong downregulation of MYC and, conversely, shMYC results in a strong downregulation of ATAD2 in this cell line, this positive feedback loop may perhaps explain the pronounced antiproliferative effects of ATAD2 knockdown in these cells. Indeed, a similar observation has been previously made in ovarian and breast cancers, in which cell lines dependent on MYC were particularly vulnerable to ATAD2 knockdown (59). Alternatively, given the well-established androgen sensitivity of LNCaP cells and

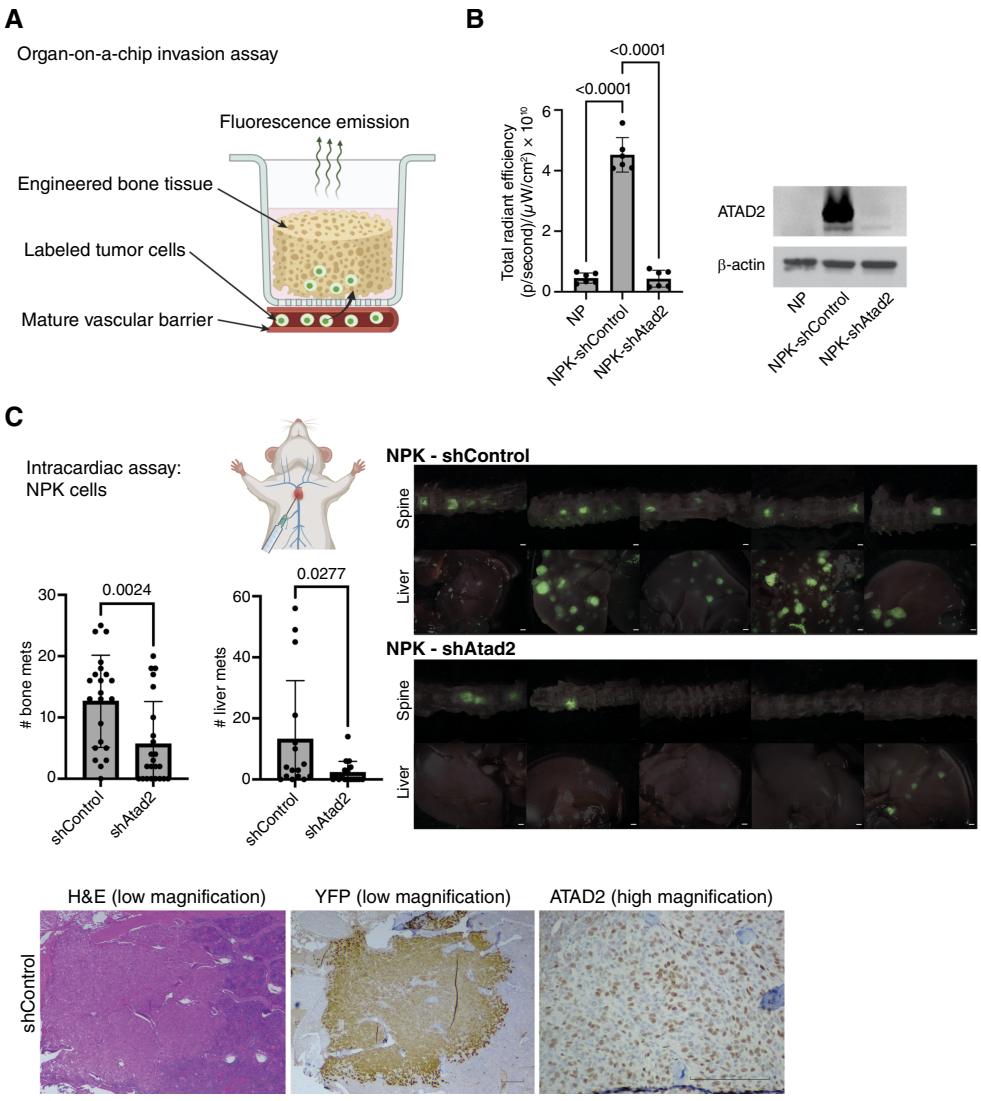

Figure 4.
ATAD2 is a driver of prostate cancer metastasis. **A,** Schematic representation of the organ-on-a-chip assay. **B,** Scatter plots showing invasion into engineered bone of indolent mouse NP cells as well as metastatic NPK cells treated with shControl or shAtad2. Corresponding expression levels of ATAD2 are shown in Western blots. *P* values are from one-way ANOVA with Dunnett multiple comparisons test, $n = 3$ technical replicates in duplicate independent experiments. **C,** Intracardiac assay after ATAD2 knockdown in *NPK* cells. Scatter plots show the number of ensuing bone (left) and liver (right) metastasis upon shControl or shAtad2 treatment of NPK cells injected intracardially into the circulation of nude mice (*P* values from two-tailed *t* test $n = 23$ in three independent experiments). Representative epifluorescence images of bones and livers are shown, in which metastases are evident by YFP fluorescence. The corresponding brightfield image of each organ is shown underneath, with opacity set to 20%. Scale bars, 0.1 cm. Representative H&E, YFP, and ATAD2 IHC staining of bone metastases ensuing from intracardiac injection of NPK shControl cells are also shown. Scale bars, 200 μm. H&E, hematoxylin and eosin; mets, metastases.

the previously reported modulation of AR signaling by ATAD2 in this context (32), further studies should address whether modulation of AR signaling is involved in preferential sensitivity to ATAD2 knockdown.

In most cancer types, ATAD2 overexpression occurs early in localized disease and is associated with poor prognosis (24, 26, 31, 34) through mechanisms involving TGF-β (27), E2F (60, 61), MYC (31), SOX10 (62), or CENPE (28). In prostate cancer, however, our study and those of others (29, 32, 34) suggest that ATAD2 overexpression occurs later in cancer progression, in a subset of advanced, metastatic tumors. Thus, understanding the common and tumor-specific mechanisms of the effects of ATAD2 on cancer progression in different cancer types or disease stages is an important area for future studies. Indeed, the few studies that have directly focused on the regulation of metastasis by ATAD2 have implicated TGF-β and CENPE pathways in metastasis to lung (27, 28). Our findings support the notion that at least in certain tumor contexts, ATAD2 may also, in turn, regulate MYC signaling, as had previously been described (31), adding to modulation of chromatin accessibility and AR signaling (32, 34) as mechanisms whereby ATAD2 promotes prostate cancer progression.

We acknowledge that metastasis is a multistep process and that ATAD2 could play a role in multiple parts of the so-called metastatic cascade. In this article, we have focused on studying its role in later stages of metastasis, once cells have entered the circulation and bone colonization. These critical steps are incompletely understood and may be particularly clinically relevant for the development of new therapeutic strategies targeting established metastasis, a currently unmet clinical need.

In summary, our article provides the first evidence that ATAD2 is linked to metastatic progression in prostate cancer and proposes ATAD2 as a promising therapeutic target.

Authors' Disclosures

M. Alshalalfa reports employment with Veracyte, Inc. E. Davicioni reports personal fees from Veracyte, Inc. during the conduct of the study and from Veracyte, Inc. outside the submitted work. R.J. Karnes reports no direct financial relationship with Veracyte, Inc. but employment with Mayo Clinic which has a

financial relationship with GenomeDx now Veracyte, Inc. No disclosures were reported by the other authors.

Authors' Contributions

A. Dutta: Formal analysis, validation, investigation. **A. Rodriguez-Calero:** Investigation. **K. Ronaldson-Bouchard:** Investigation. **A. Offermann:** Investigation. **D. Rahman:** Investigation. **T.B. Vhatkar:** Formal analysis. **D. Hasson:** Formal analysis, supervision. **M. Alshalalfa:** Resources, investigation. **E. Davicioni:** Resources. **R.J. Karnes:** Resources. **M.A. Rubin:** Supervision. **G. Vunjak-Novakovic:** Resources, supervision, writing–review and editing. **C. Abate-Shen:** Conceptualization, resources, supervision, funding acquisition, writing–original draft, writing–review and editing. **J.M. Arriaga:** Conceptualization, formal analysis, supervision, funding acquisition, investigation, writing–original draft, writing–review and editing.

Acknowledgments

J.M. Arriaga was supported by an NIH NCI K22 Award (1K22CA258806-01), a Prostate Cancer Foundation Young Investigator Award (20YOUN25), a postdoctoral training grant from the Department of Defense Prostate Cancer Research Program (W81XWH-15-1-0185), an Irving Institute/Clinical Trials Office Pilot Award funded by the National Center for Advancing Translational Sciences NIH (UL1TR001873), and the Dean's Precision Medicine Research Fellowship from the Irving Institute for Clinical and Translational Research at CUIMC (UL1TR001873). The research was supported by NIH grants R01 CA193442, R01 CA173481, R01 CA183929, and P01 CA265768 to C. Abate-Shen and UH3 EB025765, P41 EB027062, and R01 CA249799 to G. Vunjak-Novakovic. M.A. Rubin was supported by KrebsLiga Schweitz. C. Abate-Shen was supported by the TJ Martell Foundation for Leukemia, Cancer, and AIDS Research and The Prostate Cancer Foundation and is an American Cancer Society Research Professor. A. Rodriguez-Calero was supported by a Prostate Cancer Foundation Young Investigator Award. This work was supported by the Department of Defense Prostate Cancer Research Program, Award No W81XWH-18-2-0013, W81XWH-18-2-0015, W81XWH-18-2-0016, W81XWH-18-2-0017, W81XWH-18-2-0018, and W81XWH-18-2-0019 Prostate Cancer Biorepository Network (PCBN). This research was funded in part through the NIH/NCI Cancer Center Support Grant P30CA013696 awarded to the Herbert Irving Comprehensive Cancer Center (HICCC), which supported the Molecular Pathology, Flow Cytometry, Genomics and High Throughput Screening and Oncology Precision Therapeutics and Imaging Cores at HICCC. This work was supported in part by the Bioinformatics for Next Generation Sequencing (BiNGS) shared resource facility within the Tisch Cancer Institute at the Icahn School of Medicine at Mount Sinai, which is partially supported by NIH grant P30CA196521. This work was also supported in part through the computational resources and staff expertise provided by Scientific Computing at the Icahn School of Medicine at Mount Sinai and supported by the Clinical and Translational Science Awards (CTSA) grant UL1TR004419 from the National Center for Advancing Translational Sciences. Research reported in this paper was supported by the Office of Research Infrastructure of the NIH under award number S10OD026880 and S10OD030463. We would like to thank Felix Feng and Colm Morrissey for their help on our studies on patient datasets.

Note

Supplementary data for this article are available at Molecular Cancer Research Online (http://mcr.aacrjournals.org/).

Received June 13, 2024; revised December 20, 2024; accepted February 3, 2025; posted first February 5, 2025.

References

1. Siegel RL, Miller KD, Wagle NS, Jemal A. Cancer statistics, 2023. CA Cancer J Clin 2023;73:17–48.
2. Gandaglia G, Abdollah F, Schiffmann J, Trudeau V, Shariat SF, Kim SP, et al. Distribution of metastatic sites in patients with prostate cancer: a population-based analysis. Prostate 2014;74:210–6.
3. Saylor PJ, Lee RJ, Smith MR. Emerging therapies to prevent skeletal morbidity in men with prostate cancer. J Clin Oncol 2011;29:3705–14.
4. Yossepowitch O, Bianco FJ Jr, Eggener SE, Eastham JA, Scher HI, Scardino PT. The natural history of noncastrate metastatic prostate cancer after radical prostatectomy. Eur Urol 2007;51:940–7.
5. Helgstrand JT, Røder MA, Klemann N, Toft BG, Lichtensztajn DY, Brooks JD, et al. Trends in incidence and 5-year mortality in men with newly diagnosed, metastatic prostate cancer-A population-based analysis of 2 national cohorts. Cancer 2018;124:2931–8.
6. Weiner AB, Matulewicz RS, Eggener SE, Schaeffer EM. Increasing incidence of metastatic prostate cancer in the United States (2004–2013). Prostate Cancer Prostatic Dis 2016;19:395–7.
7. de Visser KE, Joyce JA. The evolving tumor microenvironment: from cancer initiation to metastatic outgrowth. Cancer Cell 2023;41:374–403.
8. Perez-Gonzalez A, Bevant K, Blanpain C. Cancer cell plasticity during tumor progression, metastasis and response to therapy. Nat Cancer 2023;4:1063–82.
9. Ganesh K, Massagué J. Targeting metastatic cancer. Nat Med 2021;27:34–44.
10. Giacobbe A, Abate-Shen C. Modeling metastasis in mice: a closer look. Trends Cancer 2021;7:916–29.
11. Arriaga JM, Abate-Shen C. Genetically engineered mouse models of prostate cancer in the postgenomic era. Cold Spring Harb Perspect Med 2019;9:a030528.
12. Vasciaveo A, Arriaga JM, de Almeida FN, Zou M, Douglass EF, Picech F, et al. OncoLoop: a network-based precision cancer medicine framework. Cancer Discov 2023;13:386–409.
13. Hubbard GK, Mutton LN, Khalili M, McMullin RP, Hicks JL, Bianchi-Frias D, et al. Combined MYC activation and Pten loss are sufficient to create genomic instability and lethal metastatic prostate cancer. Cancer Res 2016;76:283–92.
14. Cho H, Herzka T, Zheng W, Qi J, Wilkinson JE, Bradner JE, et al. RapidCaP, a novel GEM model for metastatic prostate cancer analysis and therapy, reveals myc as a driver of Pten-mutant metastasis. Cancer Discov 2014;4:318–33.
15. Arriaga JM, Panja S, Alshalalfa M, Zhao J, Zou M, Giacobbe A, et al. A MYC and RAS co-activation signature in localized prostate cancer drives bone metastasis and castration resistance. Nat Cancer 2020;1:1082–96.
16. Aytes A, Mitrofanova A, Kinkade CW, Lefebvre C, Lei M, Phelan V, et al. ETV4 promotes metastasis in response to activation of PI3-kinase and Ras signaling in a mouse model of advanced prostate cancer. Proc Natl Acad Sci U S A 2013;110:E3506–15.
17. Arriaga JM, Ronaldson-Bouchard K, Picech F, Nunes de Almeida F, Afari S, Chhouri H, et al. In vivo genome-wide CRISPR screening identifies CITED2 as a driver of prostate cancer bone metastasis. Oncogene 2024;43:1303–15.
18. Min J, Zaslavsky A, Fedele G, McLaughlin SK, Reczek EE, De Raedt T, et al. An oncogene-tumor suppressor cascade drives metastatic prostate cancer by coordinately activating Ras and nuclear factor-kappaB. Nat Med 2010;16:286–94.
19. Leibold J, Ruscetti M, Cao Z, Ho Y-J, Baslan T, Zou M, et al. Somatic tissue engineering in mouse models reveals an actionable role for WNT pathway alterations in prostate cancer metastasis. Cancer Discov 2020;10:1038–57.
20. Faltermeier CM, Drake JM, Clark PM, Smith BA, Zong Y, Volpe C, et al. Functional screen identifies kinases driving prostate cancer visceral and bone metastasis. Proc Natl Acad Sci U S A 2016;113:E172–81.
21. Labanca E, Yang J, Shepherd PDA, Wan X, Starbuck MW, Guerra LD, et al. Fibroblast growth factor receptor 1 drives the metastatic progression of prostate cancer. Eur Urol Oncol 2022;5:164–75.
22. Jia D, Zhou Z, Kwon O-J, Zhang L, Wei X, Zhang Y, et al. Stromal FOXF2 suppresses prostate cancer progression and metastasis by enhancing antitumor immunity. Nat Commun 2022;13:6828.
23. Pakula H, Omar M, Carelli R, Pederzoli F, Fanelli GN, Pannellini T, et al. Distinct mesenchymal cell states mediate prostate cancer progression. Nat Commun 2024;15:363.
24. Liu H, Wen Q, Yan S, Zeng W, Zou Y, Liu Q, et al. Tumor-promoting ATAD2 and its preclinical challenges. Biomolecules 2022;12:1040.
25. Boussouar F, Jamshidikia M, Morozumi Y, Rousseaux S, Khochbin S. Malignant genome reprogramming by ATAD2. Biochim Biophys Acta 2013;1829:1010–4.
26. Caron C, Lestrat C, Marsal S, Escoffier E, Curtet S, Virolle V, et al. Functional characterization of ATAD2 as a new cancer/testis factor and a predictor of poor prognosis in breast and lung cancers. Oncogene 2010;29:5171–81.

27. Cao L-J, Zhang Y-J, Dong S-Q, Li X-Z, Tong X-T, Chen D, et al. ATAD2 interacts with C/EBPβ to promote esophageal squamous cell carcinoma metastasis via TGF-β1/Smad3 signaling. J Exp Clin Cancer Res 2021;40:109.
28. Guruvaiah P, Chava S, Sun C-W, Singh N, Penn CA, Gupta R. ATAD2 is a driver and a therapeutic target in ovarian cancer that functions by upregulating CENPE. Cell Death Dis 2023;14:456.
29. Koo SJ, Fernández-Montalván AE, Badock V, Ott CJ, Holton SJ, von Ahsen O, et al. ATAD2 is an epigenetic reader of newly synthesized histone marks during DNA replication. Oncotarget 2016;7:70323–35.
30. Morozumi Y, Boussouar F, Tan M, Chaikuad A, Jamshidikia M, Colak G, et al. Atad2 is a generalist facilitator of chromatin dynamics in embryonic stem cells. J Mol Cell Biol 2016;8:349–62.
31. Ciró M, Prosperini E, Quarto M, Grazini U, Walfridsson J, McBlane F, et al. ATAD2 is a novel cofactor for MYC, overexpressed and amplified in aggressive tumors. Cancer Res 2009;69:8491–8.
32. Zou JX, Guo L, Revenko AS, Tepper CG, Gemo AT, Kung H-J, et al. Androgen-induced coactivator ANCCA mediates specific androgen receptor signaling in prostate cancer. Cancer Res 2009;69:3339–46.
33. Altintas DM, Shukla MS, Goutte-Gattat D, Angelov D, Rouault JP, Dimitrov S, et al. Direct cooperation between androgen receptor and E2F1 reveals a common regulation mechanism for androgen-responsive genes in prostate cells. Mol Endocrinol 2012;26:1531–41.
34. Urbanucci A, Barfeld SJ, Kytölä V, Itkonen HM, Coleman IM, Vodák D, et al. Androgen receptor deregulation drives bromodomain-mediated chromatin alterations in prostate cancer. Cell Rep 2017;19:2045–59.
35. Duan Z, Zou JX, Yang P, Wang Y, Borowsky AD, Gao AC, et al. Developmental and androgenic regulation of chromatin regulators EZH2 and ANCCA/ATAD2 in the prostate via MLL histone methylase complex. Prostate 2013;73:455–66.
36. Gurel B, Iwata T, Koh CM, Jenkins RB, Lan F, Van Dang C, et al. Nuclear MYC protein overexpression is an early alteration in human prostate carcinogenesis. Mod Pathol 2008;21:1156–67.
37. Qiu X, Boufaied N, Hallal T, Feit A, de Polo A, Luoma AM, et al. MYC drives aggressive prostate cancer by disrupting transcriptional pause release at androgen receptor targets. Nat Commun 2022;13:2559.
38. Zou M, Toivanen R, Mitrofanova A, Floch N, Hayati S, Sun Y, et al. Transdifferentiation as a mechanism of treatment resistance in a mouse model of castration-resistant prostate cancer. Cancer Discov 2017;7:736–49.
39. Irshad S, Bansal M, Castillo-Martin M, Zheng T, Aytes A, Wenske S, et al. A molecular signature predictive of indolent prostate cancer. Sci Transl Med 2013;5:202ra122.
40. Karnes RJ, Bergstralh EJ, Davicioni E, Ghadessi M, Buerki C, Mitra AP, et al. Validation of a genomic classifier that predicts metastasis following radical prostatectomy in an at risk patient population. J Urol 2013;190:2047–53.
41. Ross AE, Johnson MH, Yousefi K, Davicioni E, Netto GJ, Marchionni L, et al. Tissue-based genomics augments post-prostatectomy risk stratification in a natural history cohort of intermediate- and high-risk men. Eur Urol 2016;69:157–65.
42. Grasso CS, Wu Y-M, Robinson DR, Cao X, Dhanasekaran SM, Khan AP, et al. The mutational landscape of lethal castration-resistant prostate cancer. Nature 2012;487:239–43.
43. Varambally S, Yu J, Laxman B, Rhodes DR, Mehra R, Tomlins SA, et al. Integrative genomic and proteomic analysis of prostate cancer reveals signatures of metastatic progression. Cancer Cell 2005;8:393–406.
44. Cerami E, Gao J, Dogrusoz U, Gross BE, Sumer SO, Aksoy BA, et al. The cBio cancer genomics portal: an open platform for exploring multidimensional cancer genomics data. Cancer Discov 2012;2:401–4.
45. Cancer Genome Atlas Research Network. The molecular taxonomy of primary prostate cancer. Cell 2015;163:1011–25.
46. Abida W, Cyrta J, Heller G, Prandi D, Armenia J, Coleman I, et al. Genomic correlates of clinical outcome in advanced prostate cancer. Proc Natl Acad Sci U S A 2019;116:11428–36.
47. Kumar A, Coleman I, Morrissey C, Zhang X, True LD, Gulati R, et al. Substantial interindividual and limited intraindividual genomic diversity among tumors from men with metastatic prostate cancer. Nat Med 2016;22:369–78.
48. Ronaldson-Bouchard K, Teles D, Yeager K, Tavakol DN, Zhao Y, Chramiec A, et al. A multi-organ chip with matured tissue niches linked by vascular flow. Nat Biomed Eng 2022;6:351–71.
49. Villasante A, Marturano-Kruik A, Robinson ST, Liu Z, Guo XE, Vunjak-Novakovic G. Tissue-engineered model of human osteolytic bone tumor. Tissue Eng Part C Methods 2017;23:98–107.
50. Wang X, Kruithof-de Julio M, Economides KD, Walker D, Yu H, Halili MV, et al. A luminal epithelial stem cell that is a cell of origin for prostate cancer. Nature 2009;461:495–500.
51. The ENCODE Project Consortium; Moore JE, Purcaro MJ, Pratt HE, Epstein CB, Shoresh N, Adrian J, et al. Expanded encyclopaedias of DNA elements in the human and mouse genomes. Nature 2020;583:699–710.
52. Holmes AG, Parker JB, Sagar V, Truica MI, Soni PN, Han H, et al. A MYC inhibitor selectively alters the MYC and MAX cistromes and modulates the epigenomic landscape to regulate target gene expression. Sci Adv 2022;8:eabh3635.
53. Augello MA, Liu D, Deonarine LD, Robinson BD, Huang D, Stelloo S, et al. CHD1 loss alters AR binding at lineage-specific enhancers and modulates distinct transcriptional programs to drive prostate tumorigenesis. Cancer Cell 2019;35:603–17.e8.
54. Gilbert LA, Horlbeck MA, Adamson B, Villalta JE, Chen Y, Whitehead EH, et al. Genome-scale CRISPR-mediated control of gene repression and activation. Cell 2014;159:647–61.
55. Bamborough P, Chung C-W, Demont EH, Bridges AM, Craggs PD, Dixon DP, et al. A qualified success: discovery of a new series of ATAD2 bromodomain inhibitors with a novel binding mode using high-throughput screening and hit qualification. J Med Chem 2019;62:7506–25.
56. Fernández-Montalván AE, Berger M, Kuropka B, Koo SJ, Badock V, Weiske J, et al. Isoform-selective ATAD2 chemical probe with novel chemical structure and unusual mode of action. ACS Chem Biol 2017;12:2730–6.
57. Winter-Holt JJ, Bardelle C, Chiarparin E, Dale IL, Davey PRJ, Davies NL, et al. Discovery of a potent and selective ATAD2 bromodomain inhibitor with antiproliferative activity in breast cancer models. J Med Chem 2022;65:3306–31.
58. Yao D, Zhang J, Wang J, Pan D, He Z. Discovery of novel ATAD2 bromodomain inhibitors that trigger apoptosis and autophagy in breast cells by structure-based virtual screening. J Enzyme Inhib Med Chem 2020;35:713–25.
59. Raeder MB, Birkeland E, Trovik J, Krakstad C, Shehata S, Schumacher S, et al. Integrated genomic analysis of the 8q24 amplification in endometrial cancers identifies ATAD2 as essential to MYC-dependent cancers. PLoS One 2013;8:e54873.
60. Tong Y, Li J, Peng M, Qian Q, Shi W, Chen Z, et al. ATAD2 drives colorectal cancer progression by regulating TRIM25 expression via a positive feedback loop with E2F transcriptional factors. Biochem Biophys Res Commun 2022;594:146–52.
61. Revenko AS, Kalashnikova EV, Gemo AT, Zou JX, Chen H-W. Chromatin loading of E2F-MLL complex by cancer-associated coregulator ANCCA via reading a specific histone mark. Mol Cell Biol 2010;30:5260–72.
62. Baggiolini A, Callahan SJ, Montal E, Weiss JM, Trieu T, Tagore MM, et al. Developmental chromatin programs determine oncogenic competence in melanoma. Science 2021;373:eabc1048.